Experimental simulation of alternating aerodynamic load induced by tunnel passing of high-speed train

Qianxuan Wang[1] | Zhelong Hu[4] | Xifeng Liang[2,3] | Yitong Wu[2,3] | Wei Zhou [2,3] | Yi Yang[1] | Xiangnan Xu[1]

[1]School of Railway Tracks and Transportation, Wuyi University, Jiangmen, 529020, China

[2]School of Traffic & Transportation Engineering, Central South University, Changsha 410075, China

[3]Key Laboratory of Traffic Safety on Track (Central South University) , Ministry of Education, Changsha 410075, China

[4]KTK Group Co., Ltd, Changzhou 213102, China

Correspondce

Wei Zhou and Yitong Wu,
Key Laboratory of Traffic Safety on Track,
School of Traffic & Transportation Engineering,
Central South University, Changsha, 410075, China.
Email: zhou_wei000@126.com and 13286174280@163.com

Funding information

The 2019 Characteristic Innovation Projects of Ordinary Universities in Guangdong Province (Undergraduate), Grant/Award Number: 2019KTSCX182;
the Natural Science Foundation of Hunan Province of China, Grant/Award Number: 2020JJ4118

Abstract

Tunnel passing in high speed produces aerodynamic load on railway train, which brings about fatigue failure on the car-body, and damages passenger comfort due to interior penetration of the alternating wave. Experimental simulation of the alternating load remains a challenge concerning its accuracy and reliability. In this work, experiment approaches in terms of air compression and air suction were developed, in an attempt to simulate the air pressure variation when the train runs through tunnels. Pros and cons of the introduced methods were analyzed by theoretical calculation and numerical simulation, and further validated by experimental tests. It is revealed that in air compression means, pressure amplitude in simulation exceeds that in theoretical calculation due to temperature change from piston movement. The deviation between tests and theoretical values climbs up as the pressure wave cycle rises, which is applicable in scaled simulation for human ear comfort, but suggests insufficient engineering feasibility in full size vehicle tests. Whereas the air suction performs excellently through internal and external loading utilizing the valve controlling strategies. By simulating the pressure wave obtained from in-transit vehicle tests, the relative deviation of the extremes between simulation and vehicle tests is within 5.0%. Research outcome indicates that the proposed method provides an important experiment means for passenger comfort and car-body fatigue behavior research.

KEYWORDS

aerodynamic load, ear comfort, fatigue assessment, simulation device, vehicle body

Nomenclature

Acronyms: EMU, electric multiple unit; DAQ system, the IMC-CS1008 Data Acquisition system; Org., the original stroke; Adj., the adjusted stroke; Org.Test.Max, the maximum pressure amplitude in original piston stroke for test; Org.Simulation.Max, the maximum pressure amplitude in original piston stroke for simulation; Org.Test.Min, the minimum pressure amplitude in original piston stroke for test; Org.Simulation.Min, the minimum pressure amplitude in original piston stroke for simulation; Adj.Test.Max, the maximum pressure amplitude in adjusted piston stroke for test; Adj.Simulation.Max, the maximum pressure amplitude in adjusted piston stroke for simulation; Adj.Test.Min, the minimum pressure amplitude in adjusted piston stroke for test; Adj.Simulation.Min, the minimum pressure amplitude in adjusted piston stroke for simulation; CRH, China Railway High-speed.

Constants: V_0, the volume of enclosed air at the initial state (m^3/min); P_0, the pressure of enclosed air in eccentric propulsion at the initial state (Pa); t, the stepping motor works for a period (s); V_1, the enclosed volume (m^3/min); P_1, the enclosed air pressure (Pa); x_c, the coordinates of the piston go away from wheel connection C though the vertical x-axis; y_c, the coordinates of the piston go away from wheel connection C though the vertical y-axis; r, wheel eccentricity (mm); θ, the rotating angle of the wheel (rad); L_c, the length of crank link (mm); y_0, the initial position of the piston; y_1, the current position of the piston; d, the inner diameter of the pipeline (mm); ω, the angular speed of the wheel (rad/s); ΔP, the amplitude of pressure variation; T, the period; V_2, the enclosed volume (m^3/min); P_2, the enclosed air pressure (Pa); v, the moving speed of stepping motor (cm/s); S, the piston motion stroke (mm); L, the length of car-body model (mm); W, the width of car-body model (mm); H, the height of car-body model (mm); $y_{1\_0.5\pi}$, the piston location when $\theta = \pi/2$; $y_{1\_1.5\pi}$, the piston location when $\theta = 3\pi/2$; Δy, the amplitude of piston stroke between the valley and the peak; ΔP_{PEAK}, the pressure change at the peak; ΔP_{VALLEY}, the pressure change at the valley; S_{MAX}, the maximum extreme of pressure change when the stroke S reaches its maximum extreme; S_{MIN}, the minimum extreme of pressure change when the stroke S reaches its minimum extreme; ΔP_{MIN}, the minimum pressure change; ΔP_{MAX}, the maximum pressure change; S_0, the designed stroke amplitude between peak and valley; r_s, the solution of ratio; n_0, the initial amount of air substance in the chamber; n_1, the internal air amount and pressure during working process; V_{mol}, the air molar volume at current environmental temperature (m^3/min); Q, the air volume flow during filling or pumping (m^3/min); t_w, the working time in air suction; P1#, P2#, P3# and P4#, four pneumatic butterfly valves; C1#, C2#, C3# and C4#, 4 check valves are set beside the butterfly valves; $P(t)$, the 1st-order and 3rd-order derivative of the aerodynamic pressure curve; (P_{mi}, t_i), the magnitude and time of all extreme points of pressure time-history; P_{m1}, the initial pressure in the chamber (Pa); Q_i, the air flow volume at each stage (m^3/min); P_{sim}, the ultimate measured internal pressure (Pa); P_{exp}, the ultimate measured expected pressure (Pa); R_d, the relative deviation of P_{sim} and P_{exp}.

1 | INTRODUCTION

Safety, fastness and comfort are the three developing concerns in modern rail transit. Passenger train runs at 300 km/h in Japan and Europe, and the "Fuxing" EMU train in China operates up to 350 km/h. Higher speed brings great convenience to passengers, whereas stronger aerodynamic interaction between the train and the tunnel. A broad amount of studies have been conducted in tunnel aerodynamics theoretically and experimentally [1-4], to find its effect on the service ability of train vehicle body and tunnel facilities, as well as the passenger comfort in the train.

When a train passes through a tunnel at high speed, the air flow between tunnel wall and train exteriority, undergoes a rapid variation due to its compressibility [5,6]. The resulting pressure wave, on one hand penetrates into the vehicle body through gaps and air ducts, brings about passenger aural discomfort under internal pressure fluctuation [7,8]. On the other, it gives rise to the pressure difference between internal and external of vehicle body [9,10]. The alternating pressure variance causes hidden dangers including fatigue failure of vehicle body structures [11-13].

On passenger comfort, the internal pressure and wave velocity climb up drastically as the train speed increases when passing through tunnels. Passenger comfort and safety are seriously deteriorated. Tinnitus happens on passengers and even eardrum damage might occur [14-16]. To treat with, one important and effective means is to make speed control strategies of the train, by correlating the passenger tinnitus with internal pressure change, and train running speeds. Internal pressure change can be tested on vehicle and in laboratory. In vehicle test, it is hard to repeat the service environment in full-life cycle, and primarily of high cost. Hence, laboratory test becomes a popular way to simulate the pressure change. In 1966, an experiment was conducted to acquire the relationship between pressure fluctuation and tinnitus by using an airtight cabin in Japan [17], where the critical ear comfort line was obtained as in Figure 1. Air tight cabin tests and field tests were performed numerously in British since 1970s, to investigate the pressure variation index on passenger discomfort [18].

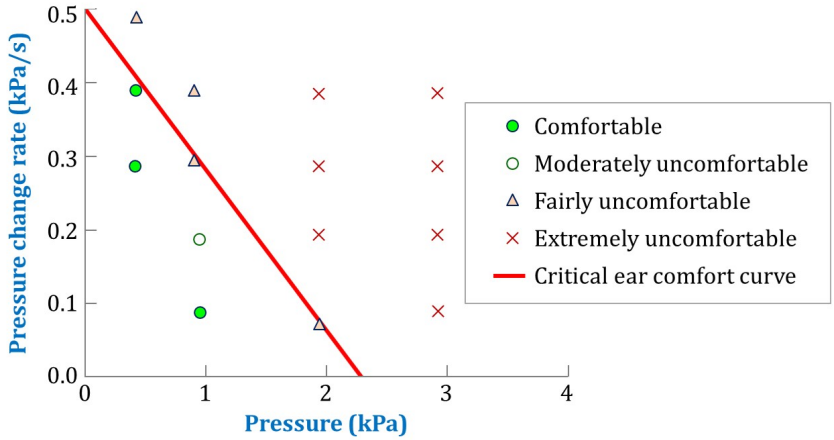

FIGURE 1 Human ear comfort curve [17]

On structural safety, tunnel pressure works on the train vehicle body in a complex way, undergoing constant propagation, reflection and superposition in the tunnel [19-21]. The pressure difference grows in high magnitude as the train speed increases. When the vehicle body is

subjected to alternating aerodynamic loads, local peak stress might occur at welding joints, discontinuous structures such as openings in compression [22]. Concentrating stress induces grain sliding and dislocation of vehicle body materials, and further initiates micro cracks on it, as in Figure 2. The micro defects propagate and develop into penetrative cracks, end in car-body fatigue fracture that endangers the safety of both the train and passengers. Relevant standards require the fatigue tests in alternating aerodynamic loads for prototype cars in European countries [23-24] and Japan [25]. In the test, triangle wave is used to act as the experiment wave form to check the fatigue strength of vehicle body.

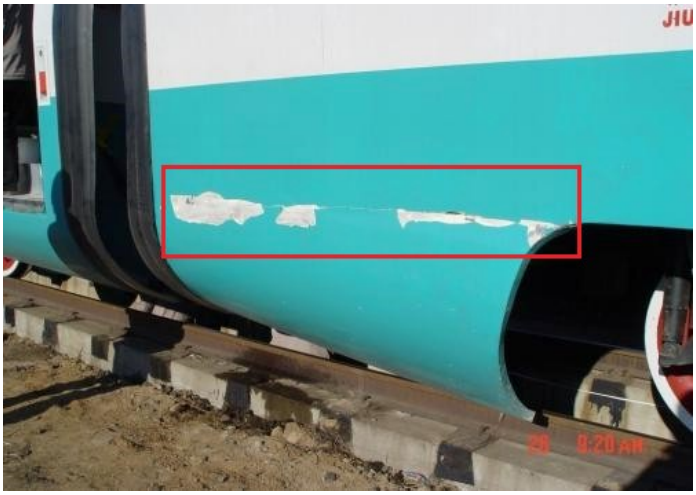

FIGURE 2 Cracks in the car-body structure

There is an exceeding advancement of China's high-speed railway in recent years, including the opening and operation of railway lines like Wuhan-Guangzhou, Beijing-Shanghai, et al. Relevant work were performed via numerical simulation on pressure wave inside the train when passing through tunnels [26-29]. But few focuses on experimental simulation of the internal pressure change. In addition, the research on aerodynamic fatigue of high-speed train is quite limited. The simplified triangle wave simulation lacks the authenticity and accuracy of the pressure wave that really occurs in tunnel passing. Hence, it is challenging to develop an experimental simulation system that can describe the complex pressure response, in an attempt to study its effect on passenger comfort and offer evidence for making measures on ear comfort in tunnel passing scenario.

In practical, the external transient pressure is delivered into the internal chamber through small gaps. Internal pressure change can be ascribed to the air flow variation at the gaps. Therefore, two ways will be introduced for experimental simulation: air compression and air suction. In air compression, the reciprocating piston is driven by stepping motor or eccentric wheel, which simulates the pressure change in terms of triangle and trigonometric wave, respectively. It offers fundamental data for passenger comfort norms under transient pressure environment in scaled car model, but lacks engineering feasibility when coming to the full-size model to assess structural fatigue behavior. The air suction uses the valve controlling strategies to realize anticipating pressure change, overcoming the difficulties in heat exchange during tests. Two ways of loading are involved in air suction, internal loading via suction inside the vehicle body, and external loading via suction in a bigger box which contains the vehicle body. Lastly, the external loading is utilized to validate the simulation precision in the work, as in Figure 3.

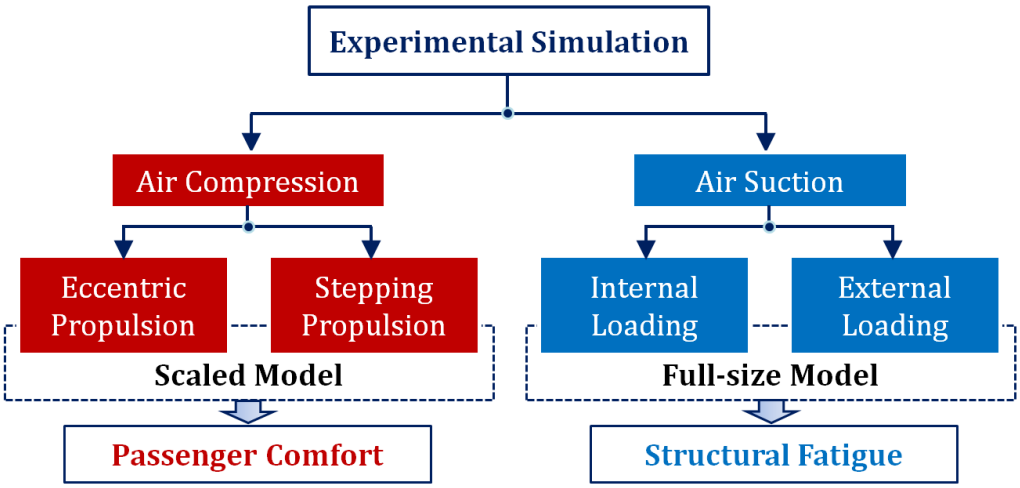

FIGURE 3 Technical route and paper framework

2 | AIR COMPRESSION METHODOLOGY

Air compression works in an air pipe, which connects to the internal vehicle body, to simulate the pressure change with reciprocating piston in the pipe. Two ways are characterized by the driving power of the piston, eccentric wheel and stepping motor. Following sections will introduce the basic principles, numerical simulations and real tests of the two proposed propulsions, respectively.

2.1 | Theoretical description

2.1.1 | Eccentric wheel propulsion

The basic principle of pressure change simulation via air compression by eccentric wheel propulsion, is depicted in Figure 4. The scaled car-body model is connected with the air pipeline. Inside the pipeline, a piston performs reciprocating movement in assistance with the crank link which connects the eccentric wheel of rotary motor, in an attempt to compress and alleviate the air in the chamber. In this way, the air volume in the car-body model undergoes constant variation, which accordingly leads to pressure change inside.

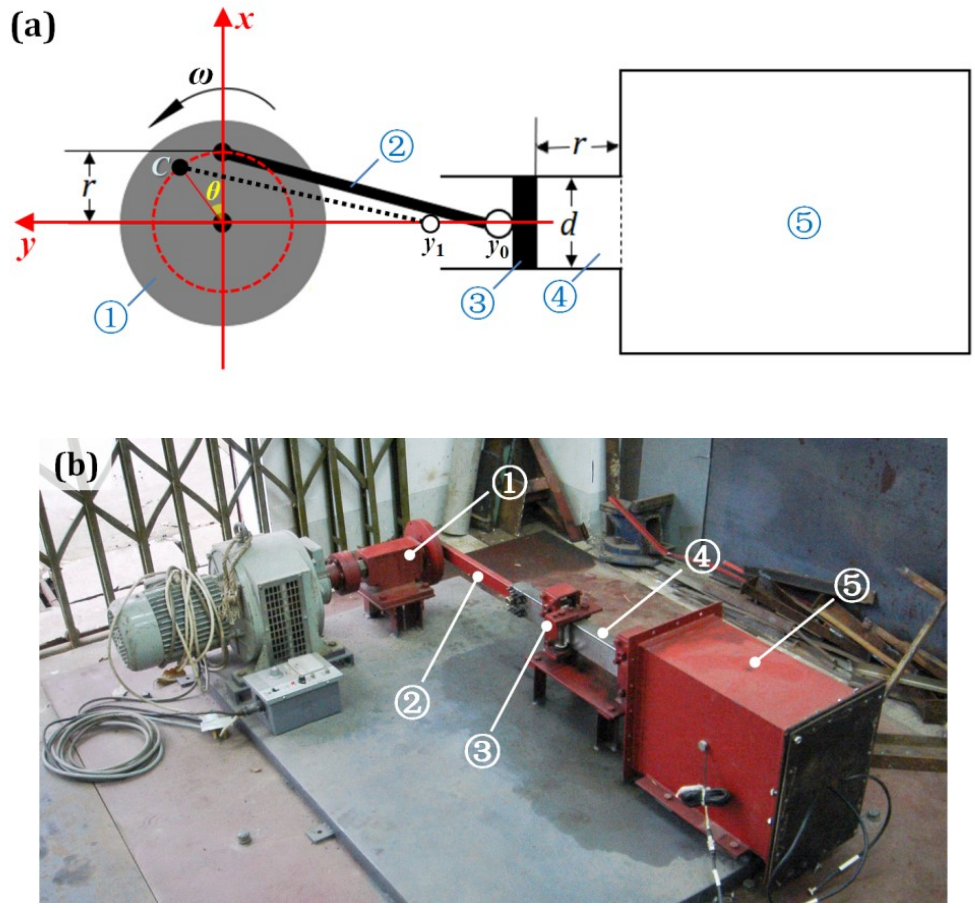

①: Eccentric wheel; ②: Crank link; ③: Reciprocating piston; ④: Pipeline; ⑤: Car-body model;

FIGURE 4 The eccentric wheel propulsion scheme: (a) schematic diagram; (b) test device

The initial state is defined at the location where the connection of crank link and eccentric wheel locates at the top, as in Figure 4(a). In initial state, the volume and the pressure of enclosed air are denoted by V_0 and P_0, respectively. As the rotary motor works for a period denoted as t. The enclosed volume and air pressure are described as V_1 and P_1, respectively. It is assumed that the inner temperature remains constant in the process. The gas state equation can be therefore given as in Equation (1).

$$P_0 \cdot V_0 = P_1 \cdot V_1 \tag{1}$$

To find the movement relation between the piston and the connection on the wheel, a coordinate system is defined at the wheel center, where the horizontal y-axis going away from the piston, the vertical x-axis pointing upward describes the positive. In the polar system, coordinates of wheel connection C can be expressed as:

$$x_C = r \cdot \cos\theta \tag{2a}$$

$$y_C = r \cdot \sin\theta \tag{2b}$$

where r is the distance between the wheel center and the connection of the crank link, θ is the rotating angle of the wheel.

Two Equation s are given by the fact that the length of crank link (denoted by L_c) remains constant respectively as (3a) in initial state and as (3b) in current state.

$$L_c{}^2 = r^2 + y_0^2 \tag{3a}$$

$$L_c{}^2 = (x_C - 0)^2 + (y_C - y_1)^2 = r^2 \cdot \cos^2\theta + (r \cdot \sin\theta - y_1)^2 \tag{3b}$$

where y_0 and y_1 are the initial and current position of the piston, respectively.

Hence, the piston position is given according to (3) as follows:

$$y_1 = r \cdot \sin\theta \pm \sqrt{L_c^2 - r^2 \cdot \cos^2\theta} \tag{4}$$

When $\theta = 0$, $y_1 = y_0$. The sign before the square term is thus negative. The volume difference between the current and the initial state of enclosed air is expressed as:

$$\Delta V = V_1 - V_0 = \frac{(y_1 - y_0)\pi d^2}{4} = \frac{\left(r \cdot \sin\theta + \sqrt{L_c^2 - r^2} - \sqrt{L_c^2 - r^2 \cdot \cos^2\theta}\right)\pi d^2}{4} \tag{5}$$

where r is the distance between the rolling center of the wheel and the connection of the crank link, d is The inner diameter of the pipeline, ω is the angular speed of the wheel.

The pressure change ΔP is then given as:

$$\Delta P = P_1 - P_0 = \left(\frac{V_0 - V_1}{V_1}\right) P_0 = \frac{\left(\sqrt{L_c^2 - r^2 \cdot \cos^2\theta} - r \cdot \sin\theta - \sqrt{L_c^2 - r^2}\right)\pi d^2}{4V_0 + \left(r \cdot \sin\theta + \sqrt{L_c^2 - r^2} - \sqrt{L_c^2 - r^2 \cdot \cos^2\theta}\right)\pi d^2} P_0 \tag{6}$$

where $\theta = \boldsymbol{\omega} \cdot \boldsymbol{t}$.

The amplitude of pressure variation ΔP in Equation (6) directly relates to the geometric parameters including the inner pipeline diameter d, the eccentricity r. The changing frequency is correlated with the angular speed ω, the period of which is calculated by $T = 2\pi/\omega$. In a testing device, the inner pipeline diameter is a fixed parameter. Thus, the eccentricity $\boldsymbol{r}$ is used to design the pressure variation amplitude, and the motor rotation speed $\boldsymbol{\omega}$ acts the role of adjusting the changing frequency.

2.1.2 | Stepping motor propulsion

Different from eccentric rotary propulsion, the stepping motor propulsion drives the piston movement via linear stepping motor. The horizontal crank links the piston and the stepping motor, which is mounted in a support that allows horizontal movement. The linear piston movement therefore results in air volume variation, followed with anticipating internal pressure change, as in Figure 5.

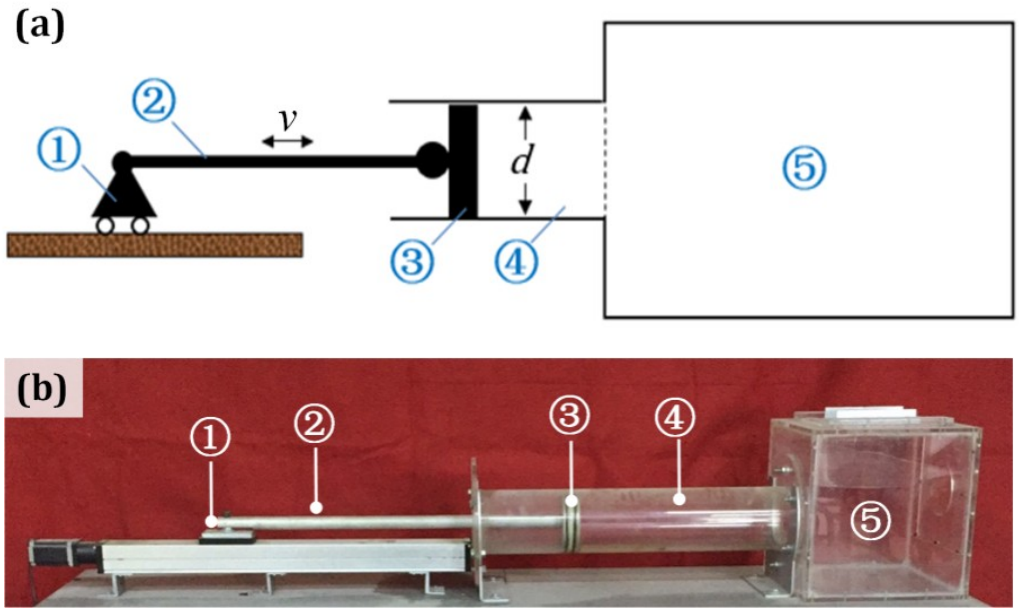

①: Stepping motor; ②: Crank link; ③: Reciprocating piston; ④: Pipeline; ⑤: Car-body model;

FIGURE 5 The stepping motor propulsion scheme: (a) schematic diagram; (b) test device

Likewise, the initial state is defined at the middle location of linear reciprocating movement. The volume and the pressure of enclosed air are denoted by V_0 and P_0, respectively as in eccentric propulsion at the initial state. As the stepping motor works for a period denoted as t. The enclosed volume and air pressure are described as V_2 and P_2, respectively. The inner temperature is supposed to remain constant in the process. The gas state equation is then given as in Equation (7).

$$P_0 \cdot V_0 = P_2 \cdot V_2 \tag{7}$$

The volume difference between the current and the initial state of enclosed air is expressed as:

$$\Delta V = V_2 - V_0 = \pi d^2 \int v\,dt/4 \tag{8}$$

where v is the moving speed of stepping motor.

Hence, the pressure change $\boldsymbol{\Delta P}$ is expressed as:

$$\Delta P = P_2 - P_0 = \left(\frac{V_0 - V_2}{V_2}\right) P_0 = \frac{-\int v\,dt}{4V_0 + \pi d^2 \int v\,dt} \pi d^2 \cdot P_0 \tag{9}$$

The pressure change amplitude $\boldsymbol{\Delta P}$ is related with geometric parameters including the internal pipeline diameter $\boldsymbol{d}$ and the motor moving speed $\boldsymbol{v}$ which determines the piston motion stroke $\boldsymbol{S}$. The changing frequency is calculated by the variation period of the speed curve of stepping motor.

2.2 | Simulation validation

In simulation, the scaled car-body model is a parallelepiped structure equipped with a hole which connects to the air pipeline. The piston in the pipeline moves in two terms respectively driven by eccentric wheel and stepping motor. Geometric parameters of the simulation device,

moving stroke and propulsion speed in eccentric propulsion and stepping propulsion are listed in Table 1 as follows:

TABLE 1 Geometric parameters and propulsion speed

Para.	Pipeline diameter d (mm)	Car-body model			Eccentric propulsion		Stepping propulsion	
		Length L (mm)	Width W (mm)	Height H (mm)	Wheel eccentricity r (mm)	Angular speed ω (2π/s)	Moving Stroke S (mm)	Linear speed v (cm/s)
Value	250	520	300	520	150	4	150	480

The simulation was carried out to investigate the inner pressure uniformity and its variation with respect to working time. The computation model includes the car-body, the pipeline and its internal piston, as in Figure 6. The initial distance between the piston and the car-body is 150 mm. In the model, the piston, pipeline and car-body are defined as non-slip wall boundaries. Unstructured grid is created with about 70,000 volume elements. To treat with the reciprocating movement of the piston, moving grid is utilized to simulate the internal pressure variation. Locations at the 6 faces and the middle of the chamber are selected as the pressure sensing positions, respectively described as 1#~7#, as in Figure 6.

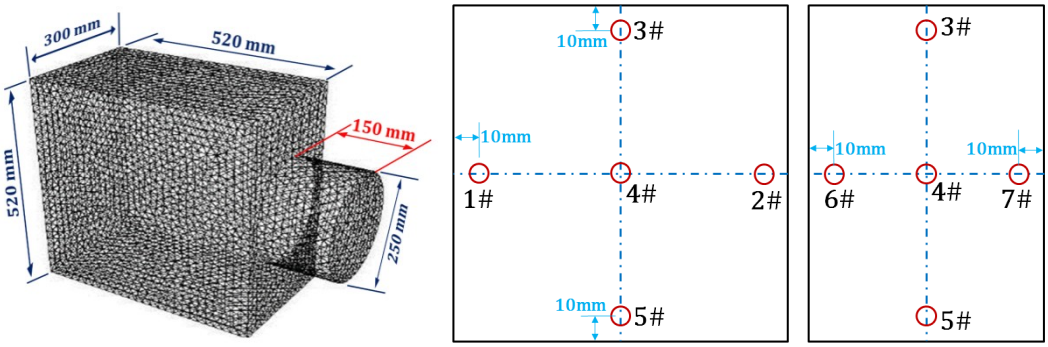

FIGURE 6 The computation model of simulation validation

According to the calculated piston movement with given parameters in Table 1 and formulation y_1-y_0 as in (5), the horizontal movement of wheel connection C and piston is shown in Figure 7(a) in eccentric propulsion, which begins at the initial rotating angle (θ=0). The stepping motor speed moves in a triangle wave where the maximum is 480 cm/s, the unit of which is set to fit in the axis range. After integration the theoretical piston movement is depicted in Figure 7(b), which starts from the leftward limit of motion range.

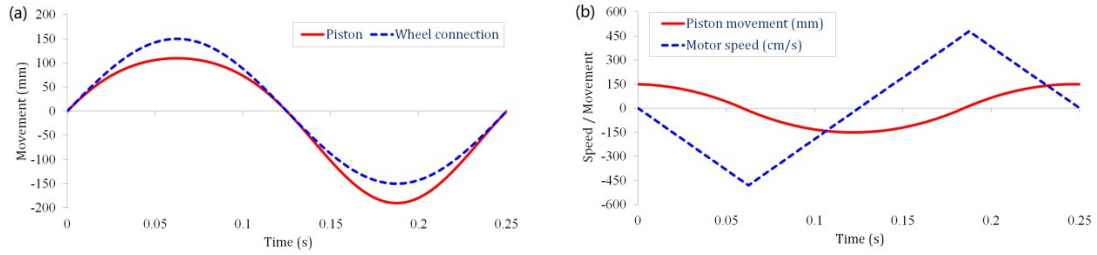

FIGURE 7 Piston movement in single working stroke: (a) Piston movement in eccentric propulsion; (b) Piston movement in stepping propulsion

Theoretical calculation reveals that in eccentric wheel propulsion, the movement of wheel connection follows a symmetric stroke in sine function, while the piston motion suggests asymmetric magnitude because of the crank link. In a stroke, the piston moves to the maximum of 109.8 mm and the minimum of -190.2 mm. This can be explained by the four locations when rotating angle θ=0, π/2, π, 3π/2. At the four locations, y_0 describes the piston location when $\theta = 0$ and π, $y_{1\_0.5\pi}$ and $y_{1\_1.5\pi}$ denotes the piston location when θ =π/2 and 3π/2, respectively. In the coordinate system defined in Figure 4(a), we have:

$$y_0 = -\sqrt{L^2 - r^2} \tag{10a}$$

$$y_{1_{0.5\pi}} = r - L \tag{10b}$$

$$y_{1_{1.5\pi}} = -r - L \tag{10c}$$

The amplitude of piston stroke between the valley and the peak is $\Delta y = y_{1\_0.5\pi} - y_{1\_1.5\pi} = 2r = 300$ mm. But the difference between the positive and negative stroke is:

$$\left(y_{1_{0.5\pi}} - y_0\right) - \left(y_0 - y_{1_{1.5\pi}}\right) = 2\sqrt{L^2 - r^2} - 2L < 0 \tag{11}$$

Above relation suggests that the negative piston stroke is constantly greater than the positive stroke, which results in the pressure difference in its increase and decrease, as well as explains the constant rotating speed of eccentric wheel gives asymmetric piston stroke.

The theoretical movement of the piston in Figure 5, is defined as the simulation input. The internal pressure change of simulation, which is calculated as the average of all 7 pressure sensing positions in the chamber, is demonstrated in four strokes versus theoretical calculation in Figure 8(a) and 8(c) respectively for eccentric and stepping propulsion. The internal temperature change under two propulsion terms are shown in Figure 8(b) and 8(d).

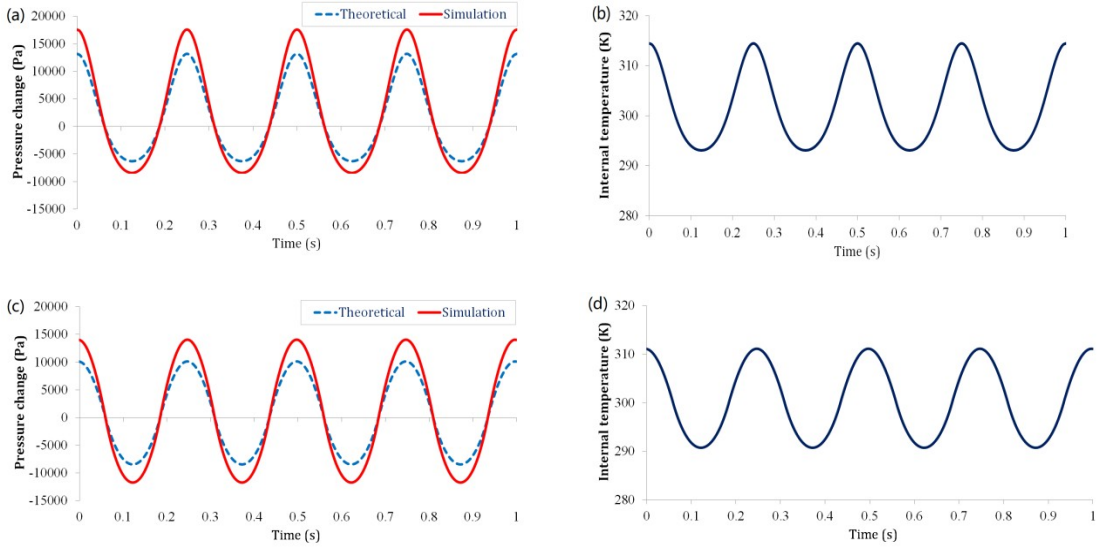

FIGURE 8 Internal pressure and temperature change in 4 working strokes: (a) Pressure change in eccentric propulsion; (b) Internal temperature change in eccentric propulsion; (c) Pressure change in stepping propulsion; (d) Internal temperature change in stepping propulsion

Simulation reveals that pressure change at the peak and the valley describes an asymmetric pattern both in eccentric wheel and stepping motor propulsion. The 7 locations (1#~7# as in Figure6) share the same internal pressure which suggests a balancing state inside the car-body model. To assess the asymmetry degree of pressure change, the asymmetry is calculated by:

$$A_{SMY}=\frac{\left|\Delta P_{PEAK}+\Delta P_{VALLEY}\right|}{\left|\Delta P_{PEAK}-\Delta P_{VALLEY}\right|}\times 100\% \tag{12}$$

where ΔP_{PEAK} and $\Delta P_{\mathrm{VALLEY}}$ are signed pressure change at the peak and the valley, respectively.

Pressure change, internal temperature at the peak and the valley are listed in Table 2 with the calculated asymmetry degree.

TABLE 2 Simulation results of air compression methodology

Parameter	Eccentric wheel propulsion			Stepping motor propulsion		
	Pressure change (Pa)		Simulation temperature (K)	Pressure change (Pa)		Simulation temperature (K)
	Theoretical	Simulation		Theoretical	Simulation	
Peak	13170.5	17682.7	314.5	10109.6	14022	311.1
Valley	-6310.2	-8024.2	293.1	-8427.8	-11189.4	290.8
Asymmetry	35.22%	37.57%	/	9.07%	11.24%	/

The asymmetry of pressure change in eccentric wheel propulsion is 3 times of that in stepping motor propulsion. Asymmetric piston stroke in eccentric wheel propulsion induces larger pressure asymmetry than symmetric piston stroke in stepping motor propulsion. However, pressure change in simulation is about 32% and 36% greater than that in theoretical calculation, respectively in eccentric and stepping propulsion. Explanation can be given according to the gas state equation when taking pressure, volume and temperature into account. In theoretical formulation, internal temperature is assumed constant, whereas in simulation the internal temperature follows a similar change as the pressure. In the gas state equation, the pressure is inversely proportional to the volume, but proportional to the temperature. When the internal temperature rises as the pressure does, it gives an increase of the pressure change compared with the adiabatic process in theoretical formulation.

In air compression, there is more that can be done for both eccentric wheel and stepping motor propulsion. The manipulative piston stroke can thereby be designed in an anticipating range in a cycle, to make pressure change at the peak and the valley the same as in (6) and (9).

To simplify the theoretical formulation, the piston stroke is expressed as S in (6) and (9). The pressure change $\boldsymbol{\Delta P}$ is therefore given as:

$$\Delta P=\frac{-\pi d^2\cdot S\cdot P_0}{4V_0+\pi d^2\cdot S}=\frac{-\pi d^2\cdot P_0}{4V_0/S+\pi d^2} \tag{13}$$

The maximum and minimum extreme of pressure change are hereby defined as S_{MAX} and S_{MIN}, which are respectively positive and negative. Apparently, when the stroke S reaches its maximum extreme S_{MAX}, the denominator in Equation (13) becomes the minimum but positive, which gives the minimum pressure change ΔP_{MIN}. Likewise, the denominator becomes the minimum but negative when the stroke S reaches its minimum extreme S_{MIN}, which gives the maximum pressure change ΔP_{MAX}. To make the peak and the valley of pressure change equal, it is required that:

$$\left|\Delta P_{MAX}\right|=\left|\Delta P_{MIN}\right| \tag{14}$$

Relation between the maximum and minimum extreme of piston stroke is given as:

$$\frac{1}{S_{MIN}}+\frac{1}{S_{MAX}}=\frac{-\pi d^2}{2V_0} \tag{15}$$

The designed stroke amplitude between peak and valley is denoted as:

$$S_0=S_{MAX}-S_{MIN} \tag{16}$$

Let $S_{MAX} = r\cdot S_0$, where r is the ratio of maximum extreme stroke to the designed stroke amplitude. Then $S_{MIN} = (r\text{-}1)\cdot S_0$. Expression of Equation (15) is then given as:

$$A\cdot r^2+(2-A)\cdot r-1=0 \tag{17}$$

where $A=\pi d^2\cdot S_0/(2V_0)$.

The solution of ratio r is formulated as:

$$r=\frac{A-2\pm\sqrt{A^2+4}}{2A} \tag{18}$$

According to the definition of ratio r, $0<r<1$. But when the sign before square part is negative and $A>2$, we have

$$A-2=\sqrt{A^2+4-4A}<\sqrt{A^2+4} \tag{19}$$

When $A<2$, the numerator is also negative, which does not satisfy the requirement of ratio range. Therefore, the maximum extreme stroke ratio is expressed as:

$$r=\frac{A-2+\sqrt{A^2+4}}{2A} \tag{20}$$

It is clear that:

$$\sqrt{A^2+4}<\sqrt{A^2+4A+4}=A+2 \tag{21}$$

Thus,

$$A-2+\sqrt{A^2+4}<2A \tag{22}$$

The inequality proves that the ratio r is in exact range from 0 to 1, when the solution selects the positive square of the two roots.

To acquire the expected asymmetric stroke, the initial piston location is adjusted 13.5 mm away from the original middle stroke as in Figure 9(a), without changing the driving parameters of eccentric wheel and stepping motor. By substituting the geometric parameters into Equation (20), the optimized stroke ratio is 54.5%. The maximum and the minimum extreme stroke, pressure change at the peak and the valley, as well as the time coverage in the peak and the valley, are listed in Table 3 and plotted in Figure 9 as follows:

TABLE 3 Calculations under optimized stroke design

Parameters	Stroke (mm)	Pressure change (Pa)			Time coverage (s)	
		Theoretical	Simulation			
			Eccentric	Stepping	Eccentric	Stepping
Peak	163.5	9118.0	12172.5	12646.4	0.10	0.11875
Valley	-136.5	-9118.0	-12172.5	-12646.8	0.15	0.13125

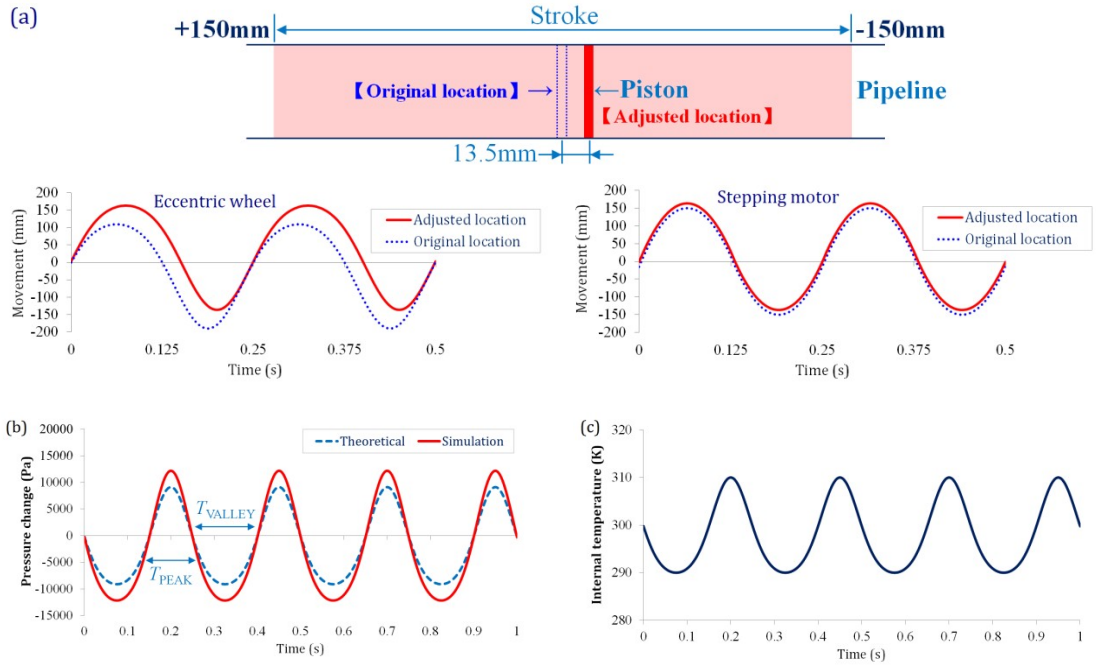

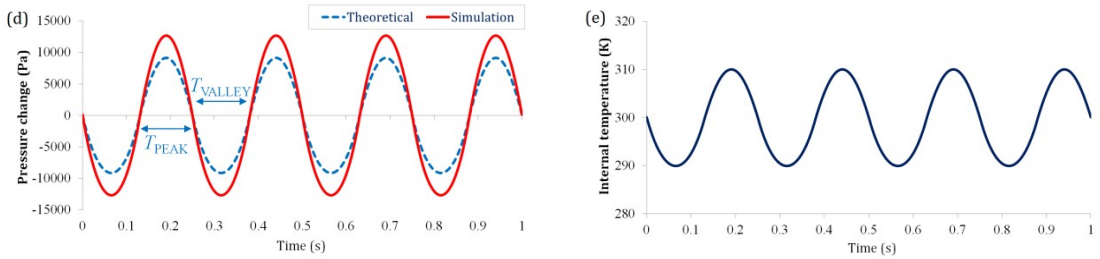

FIGURE 9 Internal pressure and temperature change under optimized stroke: (a) Adjusted piston location and optimized movement stroke; (b) Pressure change of eccentric wheel propulsion under adjusted stroke; (c) Internal temperature of eccentric wheel propulsion under adjusted stroke; (d) Pressure change of stepping motor propulsion under adjusted stroke; (e) Internal temperature of stepping motor propulsion under adjusted stroke

It is seen that by adopting the optimized piston stroke, the internal pressure change can be controlled as the anticipated symmetric variation precisely, where the peak and the valley are exactly the same. The pressure change in simulation exceeds its theoretical calculation because of internal temperature effect. As for the time coverage, the peak range which denotes air compression, is different from the valley range demonstrating air expansion, due to the initial piston location deviation. For stepping motor propulsion, the difference is as slight as within 5%, whereas climbs up to 20% for eccentric wheel propulsion. Therefore, the stepping motor propulsion has an advantage when taking the symmetric pressure change and time coverage into account.

2.3 | Experimental validation

Experimental tests were carried out on the air compression simulation facilities as in Figure 4(b) and Figure 5(b). During tests, the internal pressure was measured at three locations by pressure sensors (Honeywell-DC010) respectively centered at the top and two sides of car-body model, denoted as test point 3#, 6# and 7# as in Figure 6. The transient pressure signal was amplified and collected by the IMC-CS1008 Data Acquisition system (DAQ system).

In experimental tests, piston stroke amplitude between the peak and the valley (S_0) are defined to be 300 mm. Original piston positions when the rotating angle θ=0 for eccentric wheel propulsion, and locating at the middle stroke for stepping motor propulsion, are investigated compared with the adjusted stroke for both. Testing scenarios includes 5 moving cycles of the piston stroke, in the range from 0.1 s to 0.25s. The maximum piston speed in stepping motor propulsion is recalculated and designed as in Table 4.

TABLE 4 Testing scenarios

Scenario	Moving Cycle T (s)	Eccentric wheel			Stepping motor			Adjusted Stroke (mm)	
		Speed ω (2π/s)	Org. stroke (mm)		Speed v (cm/s)	Org. stroke (mm)			
			Peak	Valley		Peak	Valley	Peak	Valley
1#	0.250	4	109.8	-190.2	480	150	-150	163.	-136.5

								5	
2#	0.200	5	109.8	-190.2	600	150	-150	163.5	-136.5
3#	0.167	6	109.8	-190.2	718.6	150	-150	163.5	-136.5
4#	0.125	8	109.8	-190.2	960	150	-150	163.5	-136.5
5#	0.100	10	109.8	-190.2	1200	150	-150	163.5	-136.5

Note: Org. is short for “Original”.

Because the relative deviation of pressure amplitude at 3 test points (a#, b# and c#) from their average, is no more than 2.5%. The pressure change is therefore given as the average pressure difference of the 3 test points (a#, b# and c#). Pressure change in a piston stroke, characterized by the original stroke (denoted as ‘Org.’) and the adjusted stroke (denoted as ‘Adj.’), are demonstrated in Figure 10(a) and Figure 10(b) respectively for eccentric wheel and stepping motor propulsion.

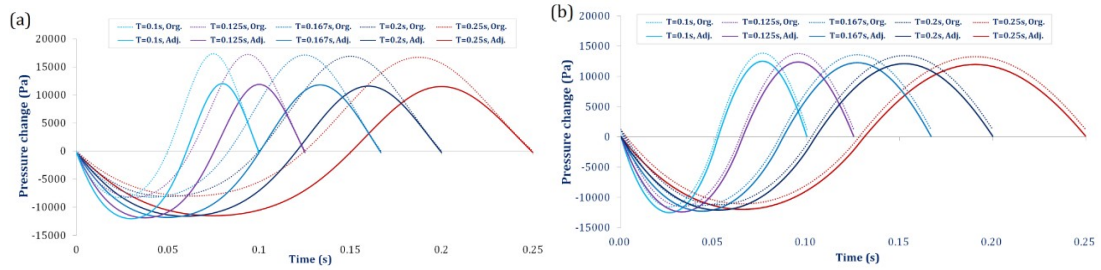

Note: Org. denotes “Original stroke” and Adj. denotes “Adjusted stroke”.

FIGURE 10 Experimental pressure change in original stroke and adjusted stroke: (a) Eccentric wheel propulsion; (b) Stepping motor propulsion

From experimental results it is seen that as the stroke cycle decreases, there is a slight increase on pressure change amplitude. To find explanations behind it, pressure amplitude in simulation remains the same in different stroke cycle for original stroke and adjusted stroke. Test results are given versus simulation in scattering plot as Figure 11, where ‘Org.Test.Max’ and ‘Org.Simulation.Max’ describe the maximum pressure amplitude in original piston stroke respectively for test and simulation, ‘Org.Test.Min’ and ‘Org.Simulation.Min’ describe the minimum pressure amplitude in original piston stroke respectively for test and simulation, ‘Adj.Test.Max’ and ‘Adj.Simulation.Max’ describe the maximum pressure amplitude in adjusted piston stroke respectively for test and simulation, ‘Adj.Test.Min’ and ‘Adj.Simulation.Min’ describe the minimum pressure amplitude in adjusted piston stroke respectively for test and simulation.

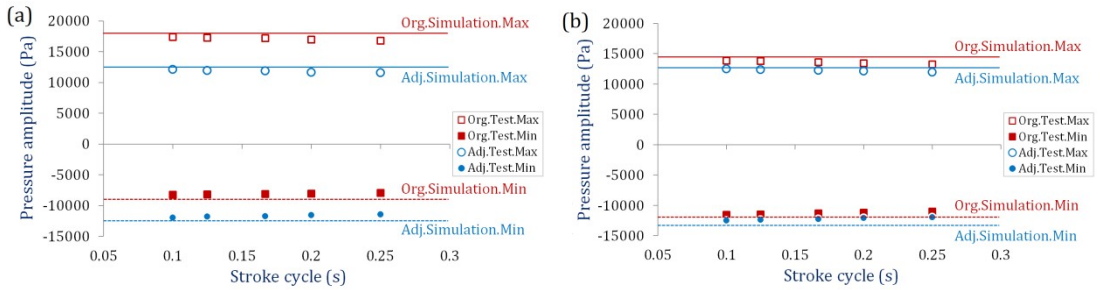

FIGURE 11 Comparison between tests and simulation in original and adjusted stroke: (a) Eccentric wheel propulsion; (b) Stepping motor propulsion

Relative deviation of test pressure amplitude from simulation, which is calculated by the ratio of its deviation to simulation amplitude, are given in terms of bar plot as Figure 12(a) and 12(b).

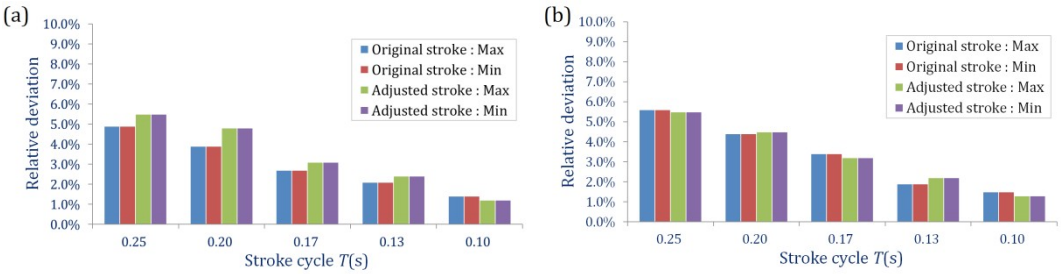

FIGURE 12 Relative deviation of pressure tests from simulation: (a) Eccentric wheel propulsion; (b) Stepping motor propulsion

It is observed that the relative tests deviation from simulation varies in the range of 1.2~5.6%. The deviation drops as the piston stroke cycle decreases. In a reduced cycle the piston moves faster, it becomes more difficult to sense the pressure loss due to airtight deficiencies of the experimental facility. However, the maximum deviation does not exceed 5.6% between tests and simulation, which proves the accuracy, reliability and its engineering feasibility. It also sheds light on simulation approaches experimentally in the field of passenger comfort evaluation, especially human ear damage assessment by using rats in scaled model under alternating pressures.

3 | AIR SUCTION METHODOLOGY

Air suction works in assistance with Roots blower, the flow is adjusted and controlled with valve groups into the full size car-body, or out of its chamber by changing the work state of valve group. The flow controlling strategy is designed in different segment, sometimes very small segments to approximate the pressure change in real running scenarios.

3.1 | Working procedure

3.1.1 | Working scheme

In air suction, the volume and temperature of car-body chamber remain unchanged. The initial amount of air substance and pressure in the chamber are demonstrated as n_0 and P_0, respectively.

The internal air amount and pressure during working process are denoted as n_1 and P_1, respectively. According to the Clapyron equation, we have

$$P_1 - P_0 = \left(\frac{n_1}{n_0} - 1 \right) P_0 \tag{23}$$

After derivation calculus to above equation, the pressure change can be given as

$$d P_1 = \frac{d n_1}{n_0} P_0 \tag{24}$$

The amount of air substance n_1 during suctioning is composed of the initial amount of air substance and the amount which is filled into or pumped out of the car-body chamber, as expressed below.

$$n_1 = \frac{V_0 + Q \cdot t}{V_{mol}} \tag{25}$$

where V_{mol} is the air molar volume at current environmental temperature, Q is the air volume flow during filling or pumping, t is the working time in air suction.

The pressure change is updated combining Equation (24) with Equation (25) as below.

$$d P_1 = \frac{Q P_0}{V_0} d t \tag{26}$$

When the air volume flow remains constant, the internal pressure can be expressed after integration to (26) as

$$P_1 = C \cdot t + D \tag{27}$$

where $C=QP_0/V_0$. The integral constant D represents the initial pressure P_0 when $t = 0$.

It is seen that the pressure changes linearly with working time when the air flow Q remains constant. From this perspective, the simulation test procedure is designed as in Figure 13(a), which is performed in a car-body of 1/3 the real vehicle size as in Figure 13(b) [29]. Two flow regulator valves are arranged at the inlet and outlet of Roots blower, providing the anticipating pressure change linearly in determined time. Four pneumatic butterfly valves, denoted by P1#, P2#, P3# and P4#, are set beside the flow regulator valves. The four valves work in two groups, P1# and P3# in one group which compresses the air in the car-body when its valves open while others close. P2# and P4# in the other group which pumps out the air when its valves are on and others are off. The two groups work in an interlocking way which ensures that when one group is turned on, the other is turned off. At the same time, 4 check valves are set beside the butterfly valves, respectively defined as C1#, C2#, C3# and C4#.

An experiment was conducted when the Roots blower works in a constant air flow at $40\mathrm{m}^3/\mathrm{min}$. The internal pressure change is measured at the top center of car-body when the two valve groups

alternatively compress and expand the internal air in every 6 seconds. The time-history of the internal pressure is shown in Figure 13(c).

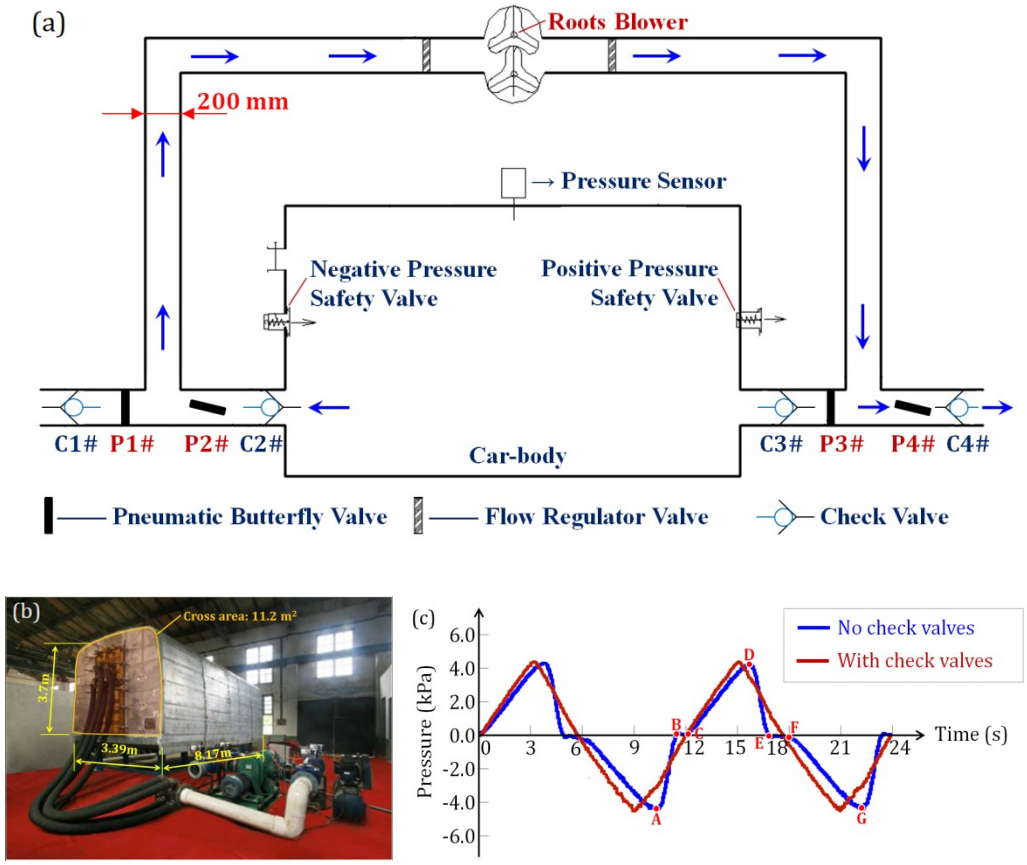

FIGURE 13 Working procedure of air suction methodology and triangle wave measurement: (a) Flow controlling strategy; (b) Real air suction devices [30]; (c) Measured internal pressure

The results are given in two terms, no or with check valves. When the pneumatic butterfly valve groups work with no check valves, an apparent distorted pressure wave is observed as the blue curve shown in Figure 13(c), because of the time taken for adjusting the valve groups from opening to complete closing, and vice versa.

During the working status adjustment of butterfly valves, at the beginning of filling right after the pumping stage as the point A shown in Figure13(c), the butterfly valve P2# and P4# begins to close, and the other group P1# and P3# starts to open. The environmental air enters in, one way to the Roots blower offering enhanced air into the car-body chamber via the opening P3#, the other way directly to the car-body chamber via the closing P2# and P4# due to the relative smaller internal pressure after pumping stage. This explains the abrupt pressure increase from A to B until the internal pressure equals that in environment, yet the two valve groups have not come to their complete open or close status. Hence a short balancing stage maintains from B to C until the valve groups completely open and close. Then, the positive pressure increase undergoes a normal way from C to D since the butterfly valves are in complete working status.

At the end of filling stage, illustrated as the point D in Figure 13(c), the valve group P2# and P4# starts to open, and the other group P1# and P3# begins to close. The air in the chamber is pumped out in this stage to decrease the internal pressure. At the beginning, the internal air moves

through the Roots blower to the environment via the opening P4, and also escapes via closing P1# and P3# to the outside environment because of the greater pressure in the chamber. Two paths give an abrupt pressure decrease from D to E until the pressure inside and outside reach a balance. The static balancing period sustains from E to F until the valve group P2# and P4# completely open, the other P1# and P3# completely close. And then, a normal decrease from F to G follows when the butterfly valves are in their complete working status.

In assistance with the check valves C1#, C2#, C3# and C4#, the environmental air no longer moves into the chamber even if the valve P2# and P4# remain half close during the filling stage because of the prevention from check valve C2# and C4#. The internal air no longer escapes to the outside through closing P1# and P3# during pumping stage because of the blocking from check valve C1# and C3#. Therefore, the application of check valves has better improved the triangle pressure waves as the red curve in Figure 13(c). The proposed scheme can be competent for creating linear pressure change at expected magnitude, as well as in anticipated time.

3.1.2 | Fitting rule

According to the air suction scheme on real vehicle-body (1/3 the vehicle length) as in Figure 13, the pressure simulation at the filling and pumping stage based on the environmental pressure P_0, is illustrated in Table 5 with the working status of butterfly valves, check valves and the calculation of air flow volume.

TABLE 5 Pressure simulation and valve working status

Stage	Filling in	Filling in	Pumping out	Pumping out
Pressure Wave	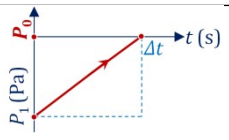	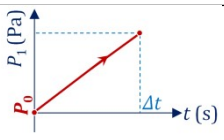	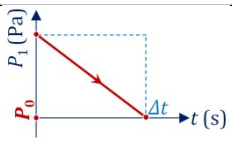	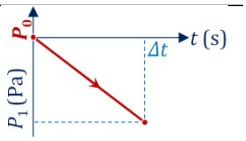
P1#	Open	Open	Close	Close
P3#	Open	Open	Close	Close
P2#	Close	Close	Open	Open
P4#	Close	Close	Open	Open
C1#	Pass	Pass	Stop	Not working
C3#	Pass	Pass	Stop	Not working
C2#	Stop	Not working	Pass	Pass
C4#	Stop	Not working	Pass	Pass
Air Flow	$\boldsymbol{Q = \lvert P_1\text{-}P_0\rvert \cdot V_0/(P_0 \cdot \Delta t)}$			

The aerodynamic pressure on vehicle body varies in a continuous, spline-shaped term according to real-vehicle tests. However in structural fatigue life estimation, only the peak and valley points, as well as their appearance time, are of interest in rainflow counting to form the load spectrum. Thus, once the aerodynamic pressure is measured in vehicle tests, following steps are introduced to fit the key points on its time history.

(1) Calculate the 1st-order and 3rd-order derivative of the aerodynamic pressure curve $P(t)$, which is the pressure difference on car-body in real vehicle test.

(2) Find all extreme points of pressure time-history by letting $P(t)'=0$ and $P(t)'''=0$. Their magnitude and time are respectively denoted as (P_{mi}, t_i), where $i=1\sim n$, n is the number of all extremes in 1st and 3rd derivatives, including the points at the start and end of the curve, as the red and blue circle in Figure 14.

(3) The initial pressure in the chamber is assumed to be P_{m1}, if not, air pumping can be utilized in designed time Δt from 0 to P_{m1}. Then, the air flow volume at each stage can be expressed as: $Q_i = |(P_{m(i+1)}-P_{mi})/(P_0+P_{mi})|\cdot V_0/(t_{i+1}-t_i)$, where P_0 is the standard air pressure of 101300 Pa, V_0 is the 1/3 car-body volume of $11.2\times8.17\text{m}^2=91.5\text{m}^2$. In each stage, the valve group P1#, P3# remains open and P2#, P4# keeps close when the internal pressure climbs up. The valve group P2#, P4# remains open and P1#, P3# keeps close when the internal pressure drops down. All check valves ensure that the pressure changes in a strict linear term.

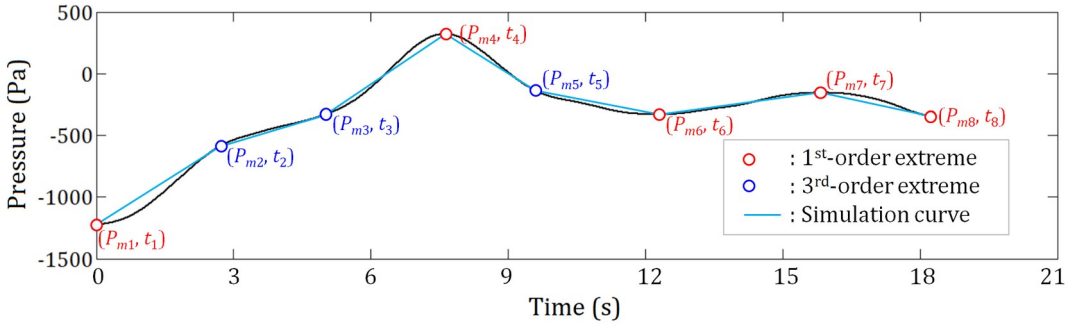

FIGURE 14 Extreme points locating and fitting strategy

3.1.3 | Loading types

The aerodynamic pressure on the car-body is the pressure difference between inside and outside. Two types of air loading are therefore proposed in terms of the location selected as the loading space, internal loading which directly fills in or pumps out the air in the car-body as in Figure 15(a), external loading which changes the pressure in a chamber and the chamber contains the sealed car-body as in Figure 15(b).

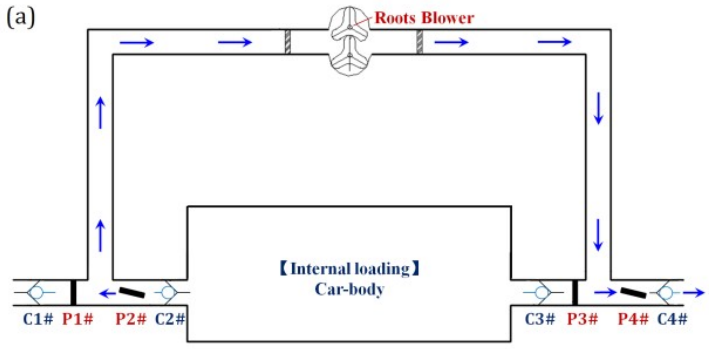

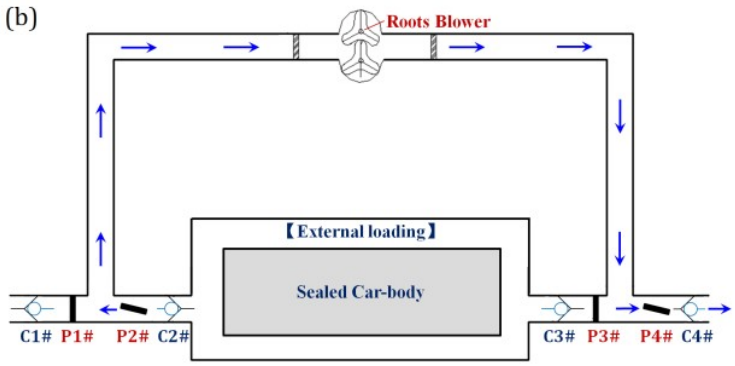

FIGURE 15 Air suction loading type: (a) Internal loading; (b) External loading

For both loading types, there is always a reference pressure in environment. The outside of car-body in internal loading, attains the standard air pressure P_0. The inside of car-body in external loading, shares the same standard air pressure P_0 with the outside of the loading chamber. In this work, the developed simulation system adopts the internal loading mode.

3.2 | Experimental application

In this part, the aerodynamic pressure on CRH train is tested by using the pressure sensors. The pressure difference of the middle vehicle is acquired when the train is passing through tunnels. Pressure responses in tunnel passing at three different tunnel lengths, are selected as the simulation targets, to validate the application of air suction methodology for real-size train vehicles.

3.2.1 | In-transit vehicle test

The in-transit vehicle test of CRH train was performed on Hefei-Wuhan railway line in 2018. The pressure measurement was conducted at the middle section on the second vehicle of the 8-car train. To make a precise test at different height, 6 pressure sensors (Honeywell-DC010, measurement range:-2.5~2.5 kPa) were set at 3 locations on both sides, vertically 1100mm, 1850mm and 3000mm from rail top, respectively. The internal pressure was measured at the middle window position at two sides, which is the common reference pressure of all external pressure sensors, as in Figure 16. Test results were collected with data acquisition equipment IMC-CS1008, and sampled at 32 Hz for the low frequency. All time-series pressure data was low-pass filtered at 10 Hz.

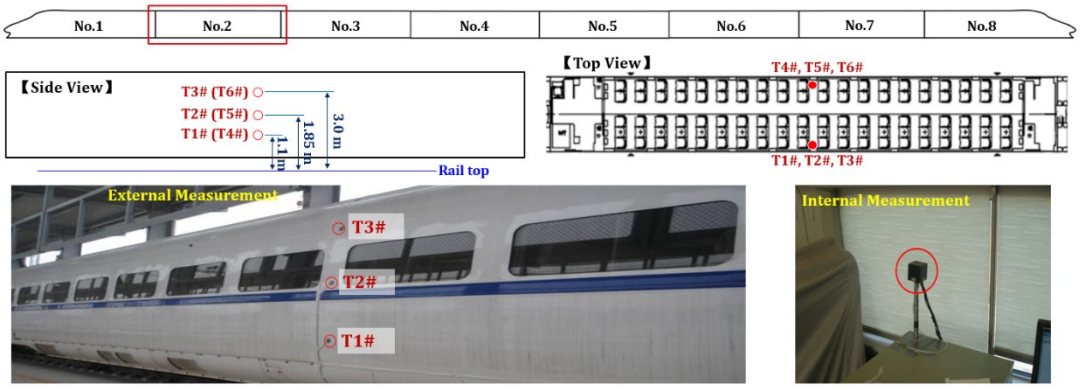

Figure 16 Vehicle test scheme and measurement

The aerodynamic pressure increases to the maximum when the train runs through tunnels. All tunnels on Hefei-Wuhan railway line are single tunnel with double tracks. The distance between lines is 4.6 m. The inner profile area of the tunnel is 92.09 m^2. When the car No.8 runs as the head car, the pressure wave on the car No.2 is tested through 3 tunnels, Yingzuishi tunnel, Tingtonggou tunnel and Hongshigeng tunnel. To get the overall pressure of the test car, the pressure response is the average of all six pressure sensors. Results including the tunnel length, passing speed, pressure peak, pressure valley and its peak-valley are illustrated in Table 6, and plotted in Figure 17.

TABLE 6 Extreme and amplitude aerodynamic load in tunnel running scenarios

Tunnel No.	Tunnel name	Tunnel length (m)	Speed (km/h)	Pressure (Pa)		
				Peak	Valley	Peak-Valley
** Expression is faulty **	Yingzuishi	1080	249	606.1	-1222	1828.1
** Expression is faulty **	Tingtonggou	2196	248	575.8	-1110	1685.8
** Expression is faulty **	Hongshigeng	5111	251	923.9	-656.6	1580.5

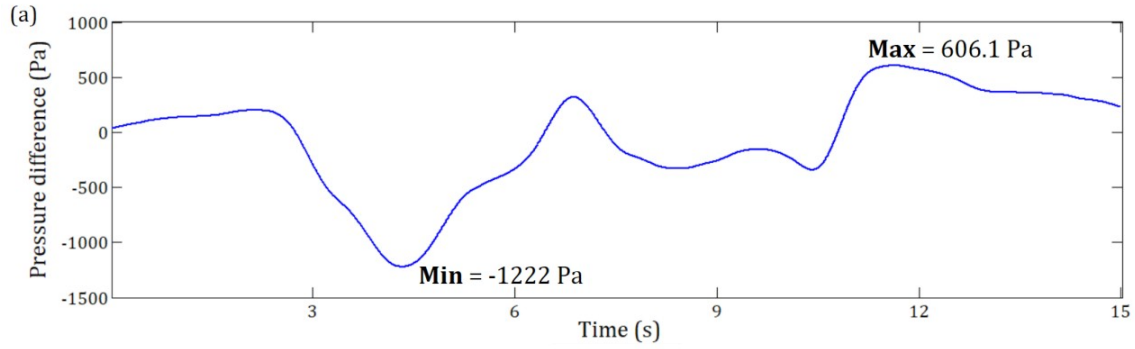

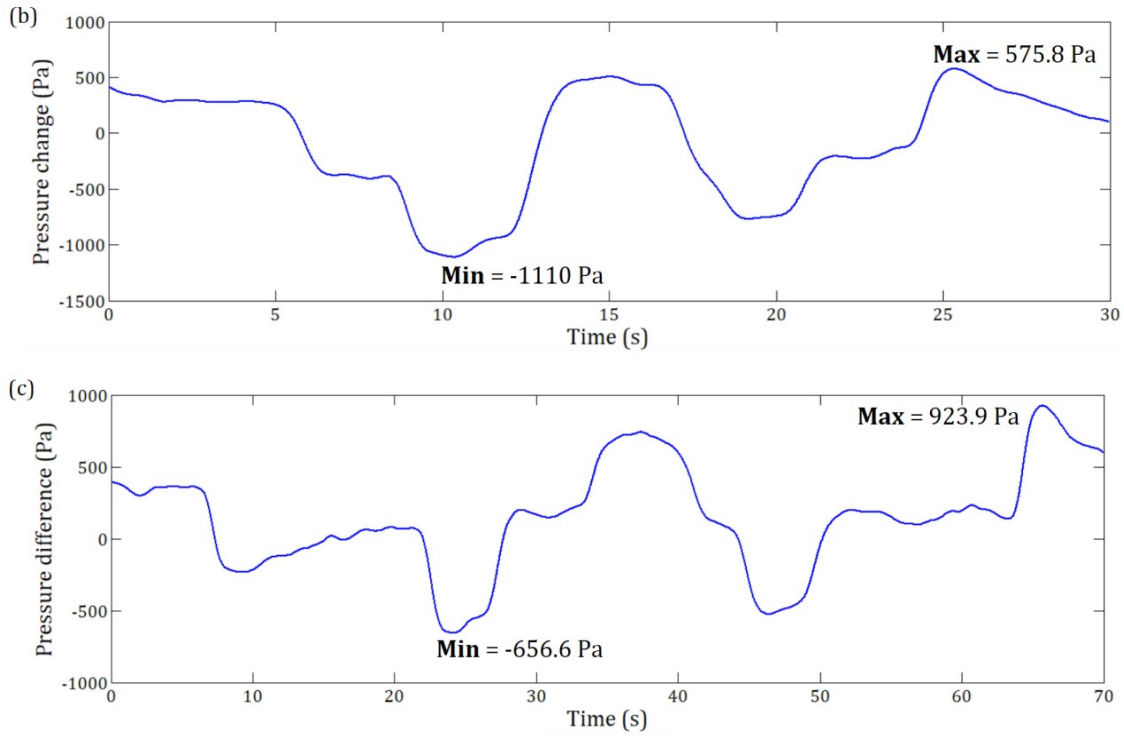

FIGURE 17 Time-history of pressure wave in different tunnel length: (a) 1080 m in tunnel length; (b) 2196 m in tunnel length; (c) 5111 m in tunnel length

Test results indicate that the tunnel length around one kilometer, arouses the biggest peak-to-valley pressure change compared with 2200-meter and 5100-meter tunnels. When the train runs at the speed of 250 km/h, the peak-to-valley pressure change reaches 1828.1 Pa, 1685.8 Pa and 1580.5 Pa respectively for tunnel length of 1080 m, 2196 m and 5111 m. The measured pressure waves will be used as the target for the experiment validation.

3.2.2 | Simulation validation

Following the fitting rule in section 3.1, the extreme points, internal loading curves can be given with the original vehicle test curves in 3 different tunnel lengths as Figure 18. The pressure difference and time interval between neighboring extremes, air flow volume in each stage, the ultimate measured internal pressure P_{sim} and expected pressure P_{exp} at the end of each stage, are listed in Table 7 to Table 9 respectively for tunnel length 1080 m, 2196 m and 5111 m. The relative deviation is calculated by: $R_d = |P_{sim}\text{-}P_{exp}|/P_{exp}\times 100\%$.

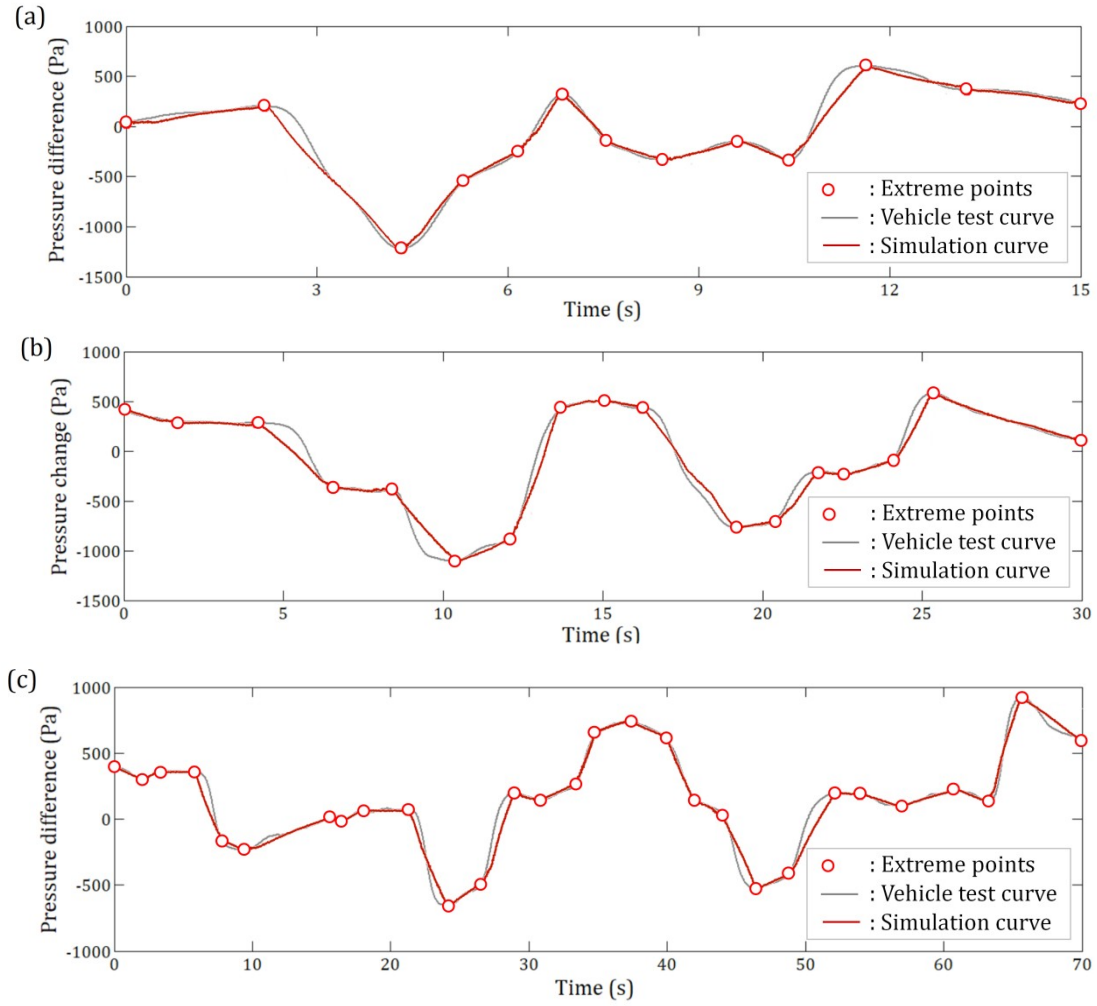

FIGURE 18 Experimental simulation results in different tunnel length: (a) 1080 m in tunnel length; (b) 2196 m in tunnel length; (c) 5111 m in tunnel length

TABLE 7 Simulation tests of the pressure wave in tunnel length: 1080 m

Stage	Pressure difference (Pa)	Time interval (s)	Air flow Volume (m^3/min)	Measured pressure P_{sim} (Pa)	Expected pressure P_{exp} (Pa)	Relative deviation
1	169.2	2.18	4.2	197.8	199.9	1.06%
2	-1421.9	2.16	35.7	-1243.6	-1222	-1.77%

3	667.3	0.96	38.1	-572.9	-554.7	-3.29%
4	268.4	0.80	18.2	-287.6	-286.3	-0.46%
5	607.0	0.78	42.5	313.5	320.7	2.23%
6	-429.8	0.61	38.1	-112.0	-109.1	-2.67%
7	-222.4	0.95	12.7	-341.2	-331.5	-2.91%
8	176.4	1.17	8.2	-154.0	-155.1	-0.68%
9	-185.8	0.80	12.5	-336.2	-340.9	-1.39%
10	947.0	1.22	42.2	584.8	606.1	3.51%
11	-241.8	1.59	8.2	365.3	364.3	0.28%
12	-132.9	1.78	4.0	238.9	231.4	3.23%

TABLE 8 Simulation tests of the pressure wave in tunnel length: 2196 m

Stage	Pressure difference (Pa)	Time interval (s)	Air flow Volume (m^3/min)	Measured pressure P_{sim} (Pa)	Expected pressure P_{exp} (Pa)	Relative deviation
1	-138.5	1.66	4.5	286.8	280.4	2.27%
2	5.2	2.50	0.1	289.0	285.6	1.18%
3	-644.8	2.33	15.0	-346.7	-359.2	-3.48%
4	-24.7	1.87	0.7	-394.9	-383.9	-2.87%
5	-726.1	2.01	19.6	-1132.0	-1110	-1.99%
6	230.5	1.72	7.3	-868.2	-879.5	-1.28%
7	1306.4	1.64	43.6	440.4	426.9	3.17%
8	78.8	1.29	3.3	494.1	505.7	2.28%
9	-74.3	1.19	3.4	439.9	431.4	1.97%
10	-1198.8	2.98	21.7	-788.6	-767.4	-2.76%
11	41.4	1.05	2.2	-736.2	-726	-1.41%
12	519.5	1.53	18.5	-213.9	-206.5	-3.57%
13	-24.3	0.74	1.8	-228.9	-230.8	-0.83%
14	128.4	1.52	4.6	-104.8	-102.4	-2.33%
15	678.2	1.30	28.3	584.4	575.8	1.49%
16	-473.6	4.67	5.5	98.8	102.2	3.35%

TABLE 9 Simulation tests of the pressure wave in tunnel length: 5111 m

Stage	Pressure difference (Pa)	Time interval (s)	Air flow Volume (m^3/min)	Measured pressure P_{sim} (Pa)	Expected pressure P_{exp} (Pa)	Relative deviation
1	-97.2	2.04	2.6	299.0	298.7	0.12%

Stage	Pressure difference (Pa)	Time interval (s)	Air flow Volume (m^3/min)	Measured pressure P_{sim} (Pa)	Expected pressure P_{exp} (Pa)	Relative deviation
2	59.1	1.30	2.5	345.5	357.8	3.43%
3	3.2	2.46	0.1	355.0	361	1.65%
4	-536.5	2.04	14.2	-180.3	-175.5	-2.72%
5	-57.8	1.49	2.1	-227.4	-233.3	-2.51%
6	252.1	6.23	2.2	18.7	18.8	0.30%
7	-28.3	0.80	1.9	-9.9	-9.483	-3.94%
8	71.2	1.64	2.4	60.7	61.67	1.60%
9	9.8	3.25	0.2	68.7	71.49	3.92%
10	-728.1	2.96	13.3	-669.7	-656.6	-1.99%
11	131.3	2.10	3.4	-514.7	-525.3	-2.02%
12	725.1	2.64	15.0	193.3	199.8	3.24%
13	-54.0	1.91	1.5	152.1	145.8	4.29%
14	105.0	2.46	2.3	254.1	250.8	1.33%
15	394.5	1.58	13.5	616.4	645.3	4.49%
16	96.7	2.48	2.1	741.2	742	0.10%
17	-122.7	2.46	2.7	605.8	619.3	2.18%
18	-461.5	2.07	12.0	156.6	157.8	0.75%
19	-110.9	2.03	3.0	48.4	46.91	3.15%
20	-572.8	2.46	12.6	-536.1	-525.9	-1.93%
21	94.8	2.27	2.3	-419.4	-431.1	-2.70%
22	629.2	3.49	9.8	205.1	198.1	3.53%
23	-11.2	1.79	0.3	179.3	186.9	4.09%
24	-89.5	3.00	1.6	99.4	97.43	1.98%
25	133.7	3.75	1.9	238.4	231.1	3.17%
26	-94.3	1.55	3.3	134.5	136.8	1.68%
27	787.1	3.45	12.3	940.5	923.9	1.80%
28	-324.1	4.30	4.0	588.6	599.8	1.88%

Simulation tests reveal that the air suction via internal loading can linearly simulate all extreme points on the pressure wave acquired from in-transit vehicle tests. For all simulations, the measured pressure difference between internal and external car-body, approximates the expected pressure on all extremes at the end of each stage. The relative deviation does not exceed 3.51%, 3.57%, 4.49% respectively for tunnel length of 1080 m, 2196 m and 5111 m. The results thus prove that the proposed air suction is an effective methodology for alternating aerodynamic load simulation, which can be helpful for aerodynamic fatigue assessment of real size vehicle-body.

4 | CONCLUSION

In this work, experiment simulation approaches in terms of air compression and air suction are proposed, so as to simulate the air pressure variation when the train runs through tunnels. Conclusions derived are as follows:

(1) Air compression alternates the air in the confined scaled model, by driving the piston in eccentric wheel or stepping motor. In simulation, the internal pressure change goes in symmetric variation in optimized piston stroke, whereas the time coverage of peak range which denotes air compression, does not equal that of valley range in air expansion. The difference between peak and valley spans is up to 20% for eccentric wheel propulsion, but as slight as within 5% for stepping motor propulsion. In laboratory tests, the relative deviation between tests and simulation does not exceed 5.6%, which proves the accuracy, reliability and feasibility of the stepping motor propulsion method. The proposed air compression, stepping motor propulsion, also inspires an experimental simulation approach in the field of passenger comfort assessment, especially human ear damage assessment by putting rats in scaled model under alternating pressures.

(2) Air suction changes the air pressure in the car-body chamber by filling in the air from environment, and pumping out the internal air to the environment. Two groups of pneumatic butterfly valves work with check valves, to linearly change the pressure at expected magnitude and in anticipated time. Fitting rules are also presented to determine the air flow volume of Roots blower, and the working status adjustment of valve groups. Two loading types are proposed according to the loading space where pressure change occurs, internal loading and external loading. Finally, the proposed air suction method is validated with in-transit vehicle test, in 3 different tunnel length when CRH2 train runs through tunnels. Results show that the relative deviation between simulation and vehicle tests goes no more than 5.0%. Research outcome indicates that the proposed method provides an important experiment means for full size car-body fatigue behavior research.

(3) In the future, it is recommended that the new car body undergo a fatigue strength test according to the actual aerodynamic load during the service process. Also, the suggested aerodynamic loading simulation method, as well as the developed system, better work with other fatigue-related tests. For example, in aerodynamic loading tests of full size vehicle-body, structural stress at key positions on matrix metals and welding joints is concurrently measured. The mechanical relation between aerodynamic pressure and structural stress can then be obtained. The stress and damage spectrum can be acquired to estimate its fatigue life.

AUTHOR CONTRIBUTION STATEMENT

Theoretical formulation: Qianxuan Wang, Zhelong Hu, Xifeng Liang and Wei Zhou;
Simulation facility design: Qianxuan Wang, Zhelong Hu, Xifeng Liang, Yitong Wu and Wei Zhou;
Simulation validation: Qianxuan Wang, Wei Zhou and Yitong Wu;
Experimental validation: Qianxuan Wang, Wei Zhou and Yitong Wu;
Acquisition and curation of data: Yitong Wu, Wei Zhou and Qianxuan Wang;
Analysis and interpretation of data: Wei Zhou, Yitong Wu and Qianxuan Wang;
Drafting of manuscript: Wei Zhou, Yitong Wu and Qianxuan Wang;
Critical revision: Yitong Wu, Wei Zhou, Qianxuan Wang, Yi Yang and Xiangnan Xu.

CONFLICT OF INTERESTS

The author(s) declared no potential conflicts of interest with respect to the research, authorship, and/or publication of this article.

ORCID iD

Wei Zhou iD https://orcid.org/0000-0001-7767-3666;
Yitong Wu iD https://orcid.org/0000-0003-2356-7109.

REFERENCES

[1] Tian HQ. Review of Research on High-Speed Railway Aerodynamics in China. *Transportation Safety and Environment*. 2019; 1: 1–21.
[2] Liu TH, Chen ZW, Xie TZ, et al. Transient loads and their influence on the dynamic responses of trains in a tunnel. *Tunnelling and Underground Space Technology*; 2017; 66: 121–133.
[3] Ma WB, Zhang QL, Liu YQ. Study evolvement of high–speed railway tunnel aerodynamic effect in China. *Journal of Traffic and Transportation Engineering*. 2012; 12(4):25–32.
[4] Chu CR, Chien SY, Wang CY, et al. Numerical simulation of two trains intersecting in a tunnel. *Tunnelling and Underground Space Technology*; 2014; 42(5): 161-174.
[5] Gilbert T, Baker C, Quinn A. Aerodynamic pressures around high–speed trains: the transition from unconfined to enclosed spaces. *Part F–Journal of Rail and Rapid Transit*. 2013; 227(6): 609–622.
[6]Miyachi T, Iida M, Fukuda T, et al. Nondimensional maximum pressure gradient of tunnel compression waves generated by offset running axisymmetric trains. *Journal of Wind Engineering and Industrial Aerodynamics*. 2016; 157: 23–35.
[7] Liu TH, Chen XD, Li WH, et al. Field study on the interior pressure variations in high–speed trains passing through tunnels of different lengths. *Journal of Wind Engineering and Industrial Aerodynamics*. 2017; 169(6): 54–66.
[8] Carpinteri A, Brighenti R, Spagnoli A. External surface cracks in shells under cyclic internal pressure. *Fatigue & Fracture of Engineering Materials & Structures*. 2000; 23(6):467-476.
[9] Zhou W, Chen L, Wang ZG, et al. Aerodynamic load spectrum and fatigue behavior of high-speed train's equipment cabin. *Fatigue & Fracture of Engineering Materials & Structures*. 2019; 42:2759-2595.
[10] Zhou W, Xiao HT, Wang ZG, et al. Dynamic target template matching for railway catenary suspension motion detection in wind area. *International Journal of Distributed Sensor Networks*. 2018; 14(9): 1-13.
[11] Zhou W, Chen L, Wang TT, et al. Deflection calculation and dynamic detection of non-uniform beam via multi-point strain measurement for freight trains. *IEEE Access*. 2019; 7:104692-104709.
[12] Wu YT, Liang XF, Zhou W, et al. Load Identification and Deflection Monitoring of Opening Beam on Well-Hole Freight Trains. *IEEE Access*. 2020; 8:86038-86056.

[13] Wang HL, Vardy AE, Pokrajac D. Perforated exit regions for the reduction of micro-pressure waves from tunnels. *Journal of Wind Engineering and Industrial Aerodynamics*. 2015; 146: 139–149.
[14] Carrarini, A. Reliability based analysis of the crosswind stability of railway vehicles. *Journal of Wind engineering and Industrial Aerodynamics*. 2007; 95(7): 493-509.
[15] Wang QX, Hu ZL, Liang XF, et al. Relationship among internal pressure, body air tightness and external pressure of rail vehicle. *Journal of Traffic and Transportation Engineering*. 2018; 18(4): 103-111.
[16] Wang QX, Liang XF, Gao GJ. Research on experimental facility of alternating aerodynamic loads of car bodies of high–speed train. *Journal of the China Railway Society*. 2013; 35(8): 29–34.
[17] Suzuki HM, Gao KY. A Review of Research Trends on Passengers' Aural Discomfort Caused by Rail Tunnel Pressure Change. *Foreign Rolling Stock*. 1999; 5: 15-18.
[18] Sun XF, Cheng Jf, Hang ZS. The summarize of High-speed train air tightness research. *Railway Vehicle*. 2004; 42(5):16-19.
[19] Zhang L., Yang MZ, Liang XF, et al. Oblique tunnel portal effects on train and tunnel aerodynamics based on moving model tests. *Journal of Wind Engineering and Industrial Aerodynamics*. 2017; 167: 128-139.
[20] Cross D, Hughes B, Ingham D, et al. A validated numerical investigation of the effects of high blockage ratio and train and tunnel length upon underground railway aerodynamics. *Journal of Wind Engineering and Industrial Aerodynamics*. 2015; 146: 195-206.
[21] BS EN 14067-5: 2006+A1: 2010. Railway application–Aerodynamics–Part 5: Requirements and test procedures for aerodynamics in tunnels.
[22] Wang LC, Zang SG, Ma JR, et al. Fatigue Loading Capacities of Side Windows on High Speed Trains. *Journal of Wuhan University of Technology*. 2010; (11): 5-8
[23] Cheng BY. The test and evaluation of high-speed passenger-carbody strength and stiffness. *Foreign Rolling Stock*. 1994; (3): 1-3.
[24] JIS E7105-1989. Test Methods for Static Load of Body Structures of Railway Rolling Stock.
[25] Sung II SEO, et al. Fatigue Strength Evaluation of Aluminium Alloy Carbody of Vehicles by Large Scale Dynamic Load Test. *Foreign Rolling Stock*. 2009; 46(2): 27-32.
[26] Niu JQ, Zhou D, Liang XF, et al. Numerical simulation of the Reynolds number effect on the aerodynamic pressure in tunnels. *Journal of Wind Engineering and Industrial Aerodynamics*. 2018; 173: 187-198.
[27] Yang QS, Song JH, Yang GW. A moving model rig with a scale ratio of 1/8 for high speed train aerodynamics. *Journal of Wind Engineering and Industrial Aerodynamics*. 2016; 152: 50-58.
[28] Yang N, Zheng XK, Zhang J, et al. Experimental and numerical studies on aerodynamic loads on an overhead bridge due to passage of high–speed train. *Journal of Wind Engineering and Industrial Aerodynamics*. 2015; 140: 19-33.
[29] Yang MZ, Tian HQ, Yuan XX. A new calculation method for micro-pressure waves induced by high-speed train passing through long tunnels and bend tunnels. *Progress in Computational Fluid Dynamics*. 2015; 15(5): 269-278.
[30] Tian HQ. Development of research on aerodynamics of high-speed rails in China. *Engineering Science*. 2015; (4): 30-41.